



Electrical conductivity as a constraint on lower mantle thermo-chemical structure



Frédéric Deschamps^{a,*}, Amir Khan^b

^a Institute of Earth Sciences, Academia Sinica, 128 Academia Road Sec. 2, Nangang, Taipei 11529, Taiwan

^b Institute of Geophysics, Swiss Federal Institute of Technology Zurich, 8092 Zurich, Switzerland

ARTICLE INFO

Article history:

Received 21 December 2015
 Received in revised form 30 May 2016
 Accepted 17 June 2016
 Available online xxxx
 Editor: J. Brodholt

Keywords:

Earth's mantle
 electrical conductivity
 mantle composition
 mantle structure
 electromagnetic C-responses

ABSTRACT

Electrical conductivity of the Earth's mantle depends on both temperature and compositional parameters. Radial and lateral variations in conductivity are thus potentially a powerful means to investigate its thermo-chemical structure. Here, we use available electrical conductivity data for the major lower mantle minerals, bridgmanite and ferropericlasite, to calculate 3D maps of lower mantle electrical conductivity for two possible models: a purely thermal model, and a thermo-chemical model. Both models derive from probabilistic seismic tomography, and the thermo-chemical model includes, in addition to temperature anomalies, variations in volume fraction of bridgmanite and iron content. The electrical conductivity maps predicted by these two models are clearly different. Compared to the purely thermal model, the thermo-chemical model leads to higher electrical conductivity, by about a factor 2.5, and stronger lateral anomalies. In the lowermost mantle (2000–2891 km) the thermo-chemical model results in a belt of high conductivity around the equator, whose maximum value reaches ~120% of the laterally-averaged value and is located in the low shear-wave velocity provinces imaged in tomographic models. Based on our electrical conductivity maps, we computed electromagnetic response functions (C-responses) and found, again, strong differences between the C-responses for purely thermal and thermo-chemical models. At periods of 1 year and longer, C-responses based on thermal and thermo-chemical models are easily distinguishable. Furthermore, C-responses for thermo-chemical model vary geographically. Our results therefore show that long-period (1 year and more) variations of the magnetic field may provide key insights on the nature and structure of the deep mantle.

© 2016 Elsevier B.V. All rights reserved.

1. Introduction

Global models of seismic tomography are converging towards a coherent picture of the mantle in the sense that different datasets and methods agree on large-scale structures (e.g. Ritsema et al., 2011). In the lowermost mantle (2400–2891 km), the seismic structure is dominated by two large low shear-wave velocity provinces (LLSVPs) beneath the Pacific and Africa, where shear-wave velocity drops by a few percent compared to its horizontally averaged value. The exact nature of LLSVPs is still unclear, but several hints suggest that they result from both thermal and chemical anomalies (e.g., van der Hilst and Kárason, 1999; Trampert et al., 2004). Alternatively, a thermally dominated origin, implying the presence of post-perovskite outside LLSVPs, has also been advocated (e.g. Davies et al., 2012). Chemical anomalies, if present, may result either from early differentiation of the Earth's

mantle, or from the recycling of oceanic crust (MORB). Calculations based on mineral physics database suggest that LLSVPs are better explained by material enriched in iron and silicate than by recycled oceanic crust, which would require temperatures in excess of 1500 K relative to average temperature at these depths (Deschamps et al., 2012). This supports a primordial origin related to early differentiation of the mantle. Following the “Basal mélange” (BAM) hypothesis (Tackley, 2012), these primordial reservoirs may however be regularly re-fed with small fractions of MORB. A major difficulty when inferring the thermo-chemical structure from seismic models, is that temperature and composition strongly trade off with one another. Efforts have been made to obtain independent constraints on the density structure from seismic normal modes (Ishii and Tromp, 1999; Trampert et al., 2004; Mosca et al., 2012), allowing the determination of large scale 3D thermo-chemical models of the mantle.

Unlike density and seismic velocities, electric conductivities of mantle minerals increase with temperature (e.g. Poirier, 1991). Earth's mantle electrical conductivity further depends on compositional parameters, in particular mineralogical composition and

* Corresponding author.

E-mail address: frederic@earth.sinica.edu.tw (F. Deschamps).

iron content. Radial profiles and 3D maps of electrical conductivity in the mantle may thus provide important information on its thermo-chemical structure (e.g. Khan et al., 2015). Such variations can be recovered from inversions of magnetic field variations recorded at geomagnetic observatories and by satellites (for a detailed treatment, see Kuvshinov and Semenov, 2012). Variations with periods from a few days to 1 year have been used to build 1D radial models of conductivity (Olsen, 1999; Kuvshinov and Olsen, 2006; Velínský, 2010; Civet et al., 2015; Puethe et al., 2015) that show an increase by 2 to 3 orders of magnitude between the top of the mantle and the core-mantle boundary. Regional and global tomographic models of mantle electrical conductivity have also been obtained (Kelbert et al., 2009; Semenov and Kuvshinov, 2012; Koyama et al., 2014). However, the 3D conductivity structures observed in these models strongly differ both in amplitude and distribution, and are limited to depths of 1600 km.

The direct approach, which consists of calculating synthetic electrical conductivity models from observed or *a priori* thermo-chemical models, provides valuable information, if these models can be tested against observations. For instance, assuming a mantle geotherm and mineralogical model, Xu et al. (2000) computed a radial conductivity profile for the entire mantle that agrees with the radial conductivity model beneath Europe obtained by Olsen (1999). More recently, Deschamps (2015) reconstructed 3D maps of conductivity from the global 3D thermo-chemical models of Trampert et al. (2004). A natural extension of the direct approach is the inversion of magnetic field data in combination with other observables for thermo-chemical models using Monte-Carlo algorithms (e.g. Khan et al., 2006; Verhoeven et al., 2009). This approach allowed recovering the radial thermo-chemical structure of the mantle at global (Verhoeven et al., 2009) and continental (Khan et al., 2006) scales. Here, using a direct approach, we calculate new 3D maps of electrical conductivity for both purely thermal and thermo-chemical models of the lower mantle, and electromagnetic response functions (C-responses) associated with these maps. Our calculations show that anomalies in electrical conductivity predicted by thermo-chemical models are stronger than those predicted using purely thermal models by a factor 2.5. At periods larger than one year, C-responses for purely thermal and thermo-chemical models are different, suggesting that long-period magnetic field variations can be used to discriminate between purely thermal and thermo-chemical models of lower mantle.

2. Modeling lower mantle electrical conductivity

At lower mantle temperature and pressure, three transport mechanisms are thought to contribute to electrical conductivity (e.g. Yoshino et al., 2009): ionic, small polaron, and proton conduction. Each mechanism involves a different charge carrier. Ionic conduction is related to the migration of Mg-site vacancies. Small polaron conduction and proton conduction involve the hopping of an electron from Fe³⁺ to Fe²⁺ ions, and the hopping of protons amongst point defects, respectively. In all three cases, however, the charge migration is a thermally activated diffusion process that follows a Boltzmann distribution, and can be described by

$$\sigma = \sigma_0 T^m \exp\left(-\frac{E_a + PV_a}{kT}\right), \quad (1)$$

where P is pressure, T is temperature, and $k = 8.617 \times 10^{-5}$ eV/m Boltzmann's constant. The exponent m appears in polaron models only (e.g. Goddat et al., 1999). The values of the pre-exponential factor σ_0 , and of the activation energy and activation volume, E_a and V_a , are different for each of the three mechanisms, and the electrical conductivity of the aggregate may be obtained by summing these three contributions. In the lower mantle, however, sev-

eral arguments indicate that small polaron conduction is the dominant mechanism, and that other mechanisms may be neglected to a good approximation. First, as pointed by Goddat et al. (1999), the activation energies of lower mantle minerals for the small polaron mechanism are small, typically a few tenths of eV, whereas for ionic conduction $E_a > 1$ eV, implying (Eq. (1)) that ionic conductivity is much smaller than small polaron. Second, because it strongly depends on the water content (Yoshino et al., 2009), proton conduction may be much less efficient in the lower mantle than in the upper mantle, since the former is thought to be dry. In this context, Xu and McCammon (2002) identified two possible mechanisms controlling the electrical conductivity of bridgmanite: ionic and small polaron. However, the conductivity obtained by summing the contributions from these two mechanisms can be parameterized with a single law (Vacher and Verhoeven, 2007). For ferropericlasite, Dobson and Brodholt (2000) identified only one regime for temperatures larger than 1000 K. Finally, Vacher and Verhoeven (2007) showed that the changes in electrical conductivity due to variations in the iron content, which may be of particular importance for the Earth's lower mantle, are much stronger than the changes induced by accounting for mechanisms with different temperature dependence.

2.1. Model and data sets

We estimated the electrical conductivity of the lower mantle aggregate following the approach underlined in Vacher and Verhoeven (2007), with some modifications. This approach considers variations due to pressure, temperature, and composition. Compositional changes include two sources: variations in mineralogical composition of the aggregate, and variations in iron fraction in each mineral composing the aggregate.

We considered a lower mantle aggregate consisting of two minerals, bridgmanite, (Mg, Fe)SiO₃, and ferropericlasite, (Mg, Fe)O. For each mineral i , the individual conductivity σ_i is given by

$$\sigma_i = \sigma_0^i \left(\frac{x_{\text{Fe}}^i}{x_{\text{ref}}^i}\right)^{\alpha_i} \exp\left[-\frac{E_a^i + \beta_i (x_{\text{Fe}}^i - x_{\text{ref}}^i) + PV_a^i}{kT}\right], \quad (2)$$

where T and P are temperature and pressure, and x_{Fe}^i , σ_0^i , and E_a^i iron fraction, pre-exponential factor, and activation energy for mineral i , respectively. The fraction of iron influences both the pre-exponential factor and the activation energy, and its effects are controlled by two parameters, α_i and β_i . Vacher and Verhoeven (2007) assume that the fractions of iron in bridgmanite and ferropericlasite, x_{Fe}^{bm} and x_{Fe}^{fp} , are equal. Here, we control these fractions by fixing the iron partitioning between bridgmanite and ferropericlasite according to

$$K_{\text{Fe}} = \frac{x_{\text{Fe}}^{bm}/(1 - x_{\text{Fe}}^{bm})}{x_{\text{Fe}}^{fp}/(1 - x_{\text{Fe}}^{fp})}. \quad (3)$$

Given the volume fraction of bridgmanite in the assemblage, X_{bm} , and global iron fraction in the aggregate,

$$X_{\text{Fe}} = X_{bm} x_{\text{Fe}}^{bm} + (1 - X_{bm}) x_{\text{Fe}}^{fp}, \quad (4)$$

the individual iron fractions x_{Fe}^{bm} and x_{Fe}^{fp} can be calculated by solving Eqs. (3) and (4). Eq. (4) indicates that x_{Fe}^{bm} increases and x_{Fe}^{fp} decreases with increasing iron partitioning. Solving Eqs. (3) and (4) further shows that for $K_{\text{Fe}} < 1.0$ both x_{Fe}^{bm} and x_{Fe}^{fp} increase with increasing fraction of bridgmanite, whereas for $K_{\text{Fe}} > 1.0$ both decrease (Supplementary Fig. S1).

To compute the bulk conductivity of the aggregate, we need to define an appropriate averaging scheme for a multiphase system.

It is usual to define several estimators based on different averaging schemes, and to compute bounds. For the latter, Hashin–Shtrikman (HS) bounds (Hashin and Shtrikman, 1962) are generally employed. HS lower (HS[−]) and upper (HS⁺) bounds are based on variational principles and are the narrowest possible bounds for a multiphase system. For a two-phase system of bridgmanite (with volume fraction X_{bm}) and ferropericlasite, and based on the observation that ferropericlasite is electrically more conductive than bridgmanite (see below), HS bounds can be computed using

$$\sigma_{HS^-} = \sigma_{bm} + \frac{(1 - X_{bm}) \sigma_{bm} (\sigma_{fp} - \sigma_{bm})}{\sigma_{bm} + X_{bm} (\sigma_{fp} - \sigma_{bm})/3}, \quad (5)$$

and

$$\sigma_{HS^+} = \sigma_{bm} - \frac{X_{bm} \sigma_{fp} (\sigma_{fp} - \sigma_{bm})}{\sigma_{fp} + (1 - X_{bm}) (\sigma_{fp} - \sigma_{bm})/3}, \quad (6)$$

where σ_{bm} and σ_{fp} are the conductivities of bridgmanite and ferropericlasite, respectively. A first estimator is given by the geometric average of the HS bounds,

$$\sigma_{HSm} = \sqrt{\sigma_{HS^-} \sigma_{HS^+}}. \quad (7)$$

Alternatively, we calculated the mean of the arithmetic and harmonic averages, or Voigt–Reuss–Hill (VRH) average (Hill, 1963),

$$\sigma_{VRH} = \frac{1}{2} \left[X_{bm} \sigma_{bm} + (1 - X_{bm}) \sigma_{fp} + \frac{\sigma_{bm} \sigma_{fp}}{(1 - X_{bm}) \sigma_{bm} + X_{bm} \sigma_{fp}} \right], \quad (8)$$

which is often used to derive the thermo-elastic properties of multiphase aggregates. This estimator is usually found to be biased towards the arithmetic average, i.e. towards the HS⁺. By contrast, the geometric average,

$$\sigma_{GM} = \sigma_{bm}^{bm} \sigma_{fp}^{(1-X_{bm})}, \quad (9)$$

is usually found to be biased towards HS[−] (e.g. Shankland and Duba, 1990; Khan and Shankland, 2012). Finally, the effective medium theory (EMT) developed by Landauer (1952) for a two-phases aggregate states provides another estimator. This theory considers each individual grain as surrounded by a homogeneous medium with conductivity σ_{EMT} . Assuming that the total polarization induced by all individual grains cancels out, σ_{EMT} satisfies a degree-two polynomial, of which it is the positive solution. For an assemblage of bridgmanite and ferropericlasite one obtains

$$\sigma_{EMT} = \frac{1}{4} \left[b + \sqrt{b^2 + 8\sigma_{bm}\sigma_{fp}} \right], \quad (10)$$

with $b = \sigma_{bm} (3X_{bm} - 1) - \sigma_{fp} (3X_{bm} - 2)$.

For calculations, we used two different data sets of the parameters governing Eq. (2). The first data set is taken from the compilation of Vacher and Verhoeven (2007) (model 1 in Table 1). In this data set, the electrical properties of bridgmanite were deduced from the mineral physics experiments of Poirier and Peyronneau (1992) and Shankland et al. (1993), and those of ferropericlasite were modeled from Dobson and Brodholt (2000). In the second data set (model 2 in Table 1), the pre-exponential factor and activation energy of bridgmanite are from Xu et al. (1998), and iron corrections are from Vacher and Verhoeven (2007). For ferropericlasite, we again employed the data of Dobson and Brodholt (2000).

Fig. 1a plots the variations of electrical conductivity with depth for an aggregate composed of 80% bridgmanite and 20% ferropericlasite using the mineral physics data set 1 in Table 1, and for two values of the iron partitioning. Both the lower and upper

Table 1

Electrical conductivity properties of bridgmanite (Bm) and ferropericlasite (Fp).

Parameter	Bridgmanite		Ferropericlasite
	Model 1	Model 2	
$\log(\sigma_0)$	1.28 ± 0.18	1.12 ± 0.12	2.56 ± 0.10
E_a (eV/K)	0.68 ± 0.04	0.62 ± 0.04	0.88 ± 0.03
V_a (cm ³ /mol)	-0.26 ± 0.03	-0.10 ± 0.03	-0.26 ± 0.07
α	3.56 ± 1.32	3.56 ± 1.32	3.14 ± 0.07
β	-1.72 ± 0.38	-1.72 ± 0.38	0
X_{ref}	0.10	0.085	0.10

In model 1, data for bridgmanite are from the Shankland et al. (1993) and Poirier and Peyronneau (1992), and iron corrections from Vacher and Verhoeven (2007). In model 2, data for bridgmanite are from Xu et al. (1998) with iron corrections again from Vacher and Verhoeven (2007). Data for ferropericlasite are from the compilation of Vacher and Verhoeven (2007), and are based on modeling of data from Dobson and Brodholt (2000) in both models 1 and 2.

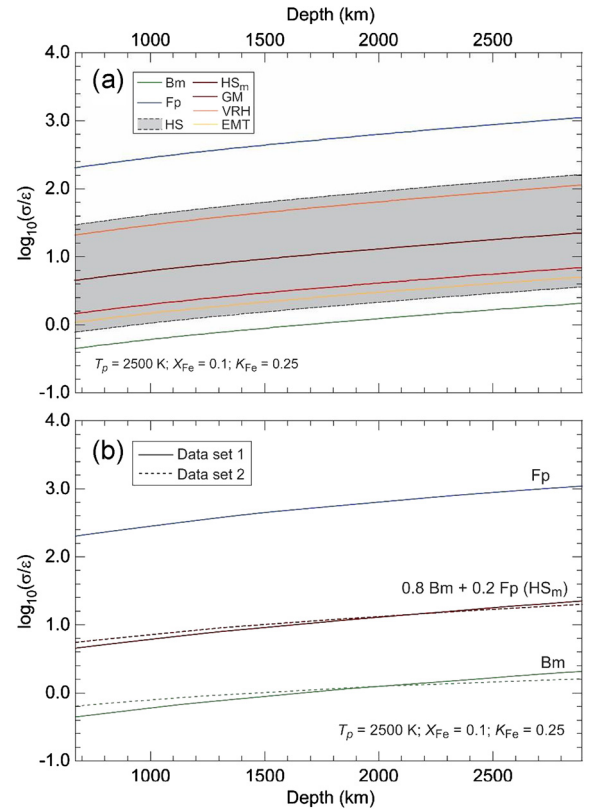


Fig. 1. Variation of electrical conductivity with depth for bridgmanite (Bm), ferropericlasite (Fp), and an assemblage of 80% bridgmanite and 20% ferropericlasite. The potential temperature is fixed to $T_p = 2500$ K, and the real temperature used to calculate the conductivity is obtained by adding an adiabatic correction to T_p . The global iron fraction is $X_{Fe} = 0.1$, and the iron partitioning $K_{Fe} = 0.25$. (a) Mineral physics data set 1 in Table 1. The extent between the lower and upper HS bounds is denoted by the grey shaded area, and four estimators are calculated: geometric average of lower and upper Hashin–Shtrikman bounds (HS_m) (Eq. (7)), geometric average (GM) (Eq. (9)), Voigt–Reuss–Hill average (VRH) (Eq. (8)), and effective medium theory (EMT) (Eq. (10)). (b) Comparison between mineral physics data set 1 (plain curves), and 2 (dashed curves) for bridgmanite (green curves) and the HS geometric average of an aggregate of 80% bridgmanite and 20% ferropericlasite (red curves). Conductivity is plotted in logarithmic scale with $\epsilon = 1.0$ S/m. (For interpretation of the references to color in this figure legend, the reader is referred to the web version of this article.)

HS bounds and the four estimators discussed above are represented. Also shown are the conductivities for bridgmanite and ferropericlasite. The input temperature is the potential temperature, T_p , and to get the real (*in situ*) temperature T_{real} , an adiabatic temperature correction must be added to T_p . We calculated this temperature correction following the data and method detailed in Deschamps and Trampert (2004). Note that, because

they partly control the value of the adiabatic bulk modulus, and thus the adiabatic gradient, the compositional parameters (X_{bm} , X_{Fe} , and K_{Fe}) indirectly influence the real temperature, and thus the electrical conductivity. For the calculations in Fig. 1, the potential temperature was fixed to $T_p = 2500$ K, leading to a real temperature at the core-mantle-boundary of about 3900 K. Fig. 1 indicates that electrical conductivity monotonically increases with depth. Again, part of this increase is related to the adiabatic increase of temperature with pressure. Another important property, already pointed out in several studies (e.g. Xu et al., 2000; Vacher and Verhoeven, 2007; Khan et al., 2006), is that ferropericase is electrically more conductive than bridgmanite throughout the lower mantle. This difference may however be substantially reduced if aluminum is present in bridgmanite (Sinmyo et al., 2014; Yoshino et al., 2016). The VRH average is close to HS+, in agreement with previous studies (e.g. Shankland and Duba, 1990; Khan and Shankland, 2012), whereas, by contrast, both the geometric and EMT averages are close to HS-. However, it is important to note that all three estimators remain within the HS bounds. An interesting property shown in Supplementary Fig. S2 is that the size of the HS interval depends on the iron partitioning. As more iron becomes incorporated into bridgmanite (increasing K_{Fe}), the difference between the individual conductivities of bridgmanite and ferropericase decreases, which in turn decreases the difference between HS- and HS+.

Fig. 1b compares the electrical conductivity of bridgmanite and of the HS geometric average (Eq. (7)) for an aggregate of 80% bridgmanite and 20% ferropericase obtained with the two data sets listed in Table 1. The electrical conductivity of ferropericase, which is calculated using the same data in our two models, is shown for comparison. The largest discrepancies in the conductivities of bridgmanite and of the aggregate are in the top part of the lower mantle (<1200 km). Around 2000 km depth, the conductivities calculated with the two data sets are very similar, and in the lowermost mantle, discrepancies increase slightly. For example, at 2800 km depth, the conductivities for the aggregate obtained with data sets 1 and 2 differ by 2.0 S/m, i.e. about 10% in relative value. Other estimators also lead to relatively small-to-moderate differences in the lower mantle, up to about 20% in the case of EMT. Differences in the calculated conductivities for data sets 1 and 2 are not substantially affected by the thermo-chemical input parameters.

2.2. Influence of temperature and composition

Electrical conductivity increases with increasing real temperature (i.e. the potential temperature plus the adiabatic contribution) throughout the lower mantle (Fig. 2a), this increase being attenuated with increasing pressure (depth). Raising the temperature from 2000 to 4000 K induces an increase in electrical conductivity by a factor 4 at 2000 km depth, and by only a factor of 2.5 at 2800 km. Fig. 2a further indicates that a temperature excess of 500 K at the bottom of the mantle, as might be the case in LLSVPs (Trampert et al., 2004; Mosca et al., 2012) would result in a change in electrical conductivity between 15 and 25%, depending on the mantle reference temperature.

Small polaron conduction is related to charge hopping from Fe^{3+} to Fe^{2+} ions and is therefore strongly sensitive to variations in the iron content, with electrical conductivity increasing as the fraction of iron increases (Fig. 2b). In the lowermost mantle, and for $X_{bm} = 0.8$ and $K_{Fe} = 0.25$, increasing X_{Fe} by 4%, which is typical of the enrichment expected in LLSVPs (Trampert et al., 2004; Mosca et al., 2012), induces a three-fold increase in conductivity. Note that increasing iron partitioning enhances the influence of iron, but does not modify the trend, i.e. electrical conductivity

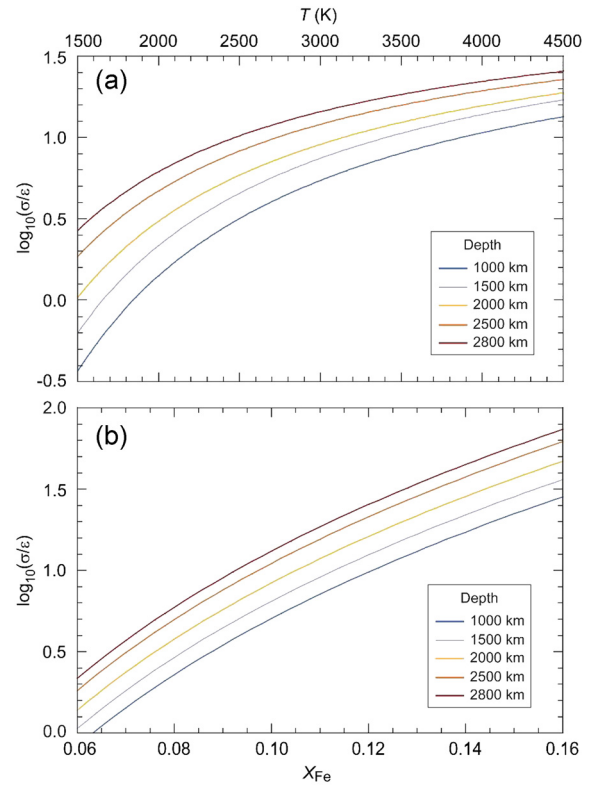


Fig. 2. Influence of (a) temperature and (b) global fraction of iron, X_{Fe} , on the conductivity of the aggregate. The volume fraction of bridgmanite and iron partitioning are $X_{bm} = 0.8$ and $K_{Fe} = 0.25$, respectively, and the electrical properties are from data set 1 in Table 1. In plot (a), the global iron fraction is $X_{Fe} = 0.1$, and in plot (b) the real temperature is $T_{real} = 3000$ K. Averaging scheme is geometric average of the upper and lower Hashin–Shtrikman bounds, and several depths are considered (legend). Conductivity is plotted in logarithmic scale with $\varepsilon = 1.0$ S/m. (For interpretation of the references to color in this figure legend, the reader is referred to the web version of this article.)

increases with increasing iron fraction whatever the value of iron partitioning.

Since bridgmanite is less conductive than ferropericase throughout the lower mantle, the electrical conductivity of the mantle aggregate should decrease with increasing fraction of bridgmanite, X_{bm} . However, because the sensitivity to iron fraction is different for bridgmanite and for ferropericase (Table 1), the detailed influence of the fraction of X_{bm} is more complex, and depends on the value of the iron partitioning, K_{Fe} , and on the averaging scheme (Fig. 3). For $K_{Fe} = 1.0$ the fractions of iron in bridgmanite and ferropericase are equal, and the electrical conductivity decreases with increasing X_{bm} independently of the averaging scheme employed (Fig. 3a). We observe a similar trend for $K_{Fe} > 1.0$, and for values of K_{Fe} down to 0.5 (Fig. 3b). For $K_{Fe} < 0.5$, relevant to Earth's lower mantle, the influence of X_{bm} is more complex (Figs. 3c and 3d). For instance, if $K_{Fe} = 0.2$, the conductivity predicted by the HS geometric average first sharply decreases from $X_{bm} = 0.0$ to $X_{bm} = 0.2$, then slowly increases up to $X_{bm} = 0.9$, and decreases again up to $X_{bm} = 1.0$. Interestingly, for values relevant to the Earth's mantle, i.e. $X_{bm} > 0.7$, the volume fraction of bridgmanite has only a moderate influence on the electrical conductivity. For $0.2 \leq K_{Fe} \leq 0.4$, a rise of X_{bm} from 0.8 to 0.9 changes the conductivity by 10 to 20%, depending on the averaging scheme.

The results displayed in Figs. 2 and 3 indicate that regions of the mantle that are hotter than average and/or enriched in iron, as might be the case of the LLSVPs (Trampert et al., 2004; Deschamps et al., 2012; Mosca et al., 2012), should be electrically more conductive than the surrounding regions. Additional increase in the relative volume fraction of silicate may slightly reduce or

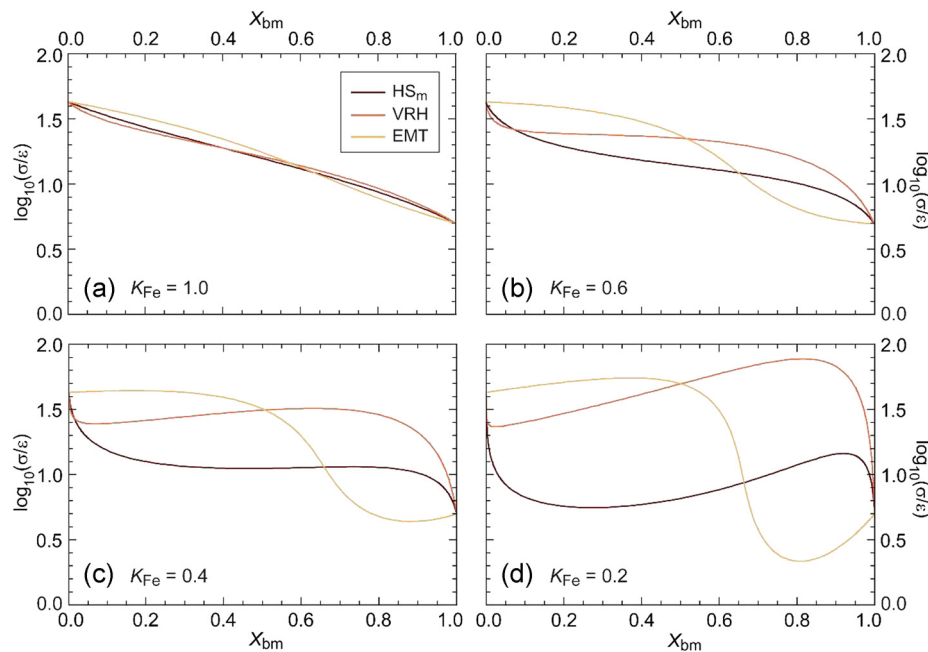


Fig. 3. Combined influence of the volume fraction of bridgmanite, X_{bm} , and the iron partitioning, K_{Fe} , on the conductivity of the aggregate. Results are plotted as a function of X_{bm} and for (a) $K_{Fe} = 1.0$, (b) $K_{Fe} = 0.6$, (c) $K_{Fe} = 0.4$, and (d) $K_{Fe} = 0.2$. Three estimators are shown: geometric average of the upper and lower Hashin–Shtrikman bounds (HS_m), Voigt–Reuss–Hill average (VRH), and effective medium theory (EMT). All calculations are made with mineralogical data set 1 at 2500 km depth, real temperature $T_{real} = 3000$ K, and global iron fraction $X_{Fe} = 0.1$. Conductivity is plotted in logarithmic scale with $\varepsilon = 1.0$ S/m.

increase this trend. These implications are further discussed and quantified in the next section.

3. Lower mantle electrical conductivity inferred from probabilistic tomography

Lateral variations in mantle temperature and composition trigger variations in seismic velocity anomalies with comparable amplitude. Thermal and compositional contributions to seismic velocity anomalies are however difficult to separate. Tomographic models that provide independent distributions of relative shear-wave and bulk-sound velocity anomalies show that these two distributions are anti-correlated (Ishii and Tromp, 1999; Masters et al., 2000; Trampert et al., 2004). This strongly suggests that these regions are both thermally and compositionally different from the surrounding mantle, but a thermally dominated explanation may not be completely ruled out (Davies et al., 2012). The de-correlation between shear-wave velocity and density anomalies, as mapped by probabilistic tomography, provides another strong hint for a thermo-chemical variations. Models of probabilistic tomography, which are based on a Monte-Carlo inversion, further allow mapping thermal and compositional variations in the deep mantle (Trampert et al., 2004; Mosca et al., 2012), indicating that LLSVPs are enriched in iron and silicate, relative to the average mantle.

Differences in lower mantle thermo-chemical structures will result in different distributions of electrical conductivity. Here, we considered two models: a purely thermal model deduced from the shear-wave velocity anomalies of probabilistic tomography of Trampert et al. (2004) with sensitivities to temperature also from Trampert et al. (2004); and the 3D thermo-chemical model of Trampert et al. (2004), consisting of anomalies in temperature, iron, and silicate (parameterized as variations in the volume fraction of (Mg, Fe)-bridgmanite). This model is radially parameterized in three layers in the lower mantle: 670–1200 km, 1200–2000 km, and 2000–2891 km. A more recent 3D thermo-chemical model, with thinner radial parameterization and including distribution in the post-perovskite phase, is available (Mosca et al., 2012). How-

ever, because electrical conductivity data for post-perovskite are still sparse, we preferred to use the thermo-chemical distributions of Trampert et al. (2004).

At each point of the purely thermal and thermo-chemical models, and for each of the two mineral physics data sets in Table 1, we calculated the HS bounds of the aggregate electrical conductivity (Eqs. (5) and (6)), and the four estimators outlined in section 2.1 (Eqs. (7) to (10)). Mineral physics parameters are varied within their uncertainties and the iron partition coefficient is randomly varied in the range 0.2–0.5. The relative thermo-chemical distributions are varied within their error bars and added to the 1D radial thermo-chemical model DT2 of Deschamps and Trampert (2004), which is also varied within its error bars. In DT2, the average potential temperature is around 2000 K, with uncertainties (taken as one standard deviation around the average temperature) of ~ 500 K, leading to a real temperature (*i.e.* including the adiabatic correction) at the bottom of the mantle in the range 2700–3700 K. The reference fraction of iron is nearly constant with depth, around 0.09 ± 0.02 , and the reference fraction of bridgmanite varies between 0.7 and 0.8 (with uncertainty ~ 0.1), depending on depth. Note that for the purely thermal model, reference iron and bridgmanite fractions are fixed for each layer, and only the reference temperature is varied within error bars. Calculations are performed on a $15 \times 15^\circ$ grid, corresponding to the original node parameterization of Trampert et al. (2004). At each depth, we consider a total of 10^4 different thermo-chemical models and 10^5 combinations of mineral physics parameters, leading to a collection of models of electrical conductivity from which the mean and standard deviation are calculated.

Results for data set 1 are shown in Fig. 4 (1D horizontally averaged models), and Figs. 5 and 6 (HS geometric average, Eq. (7)). Results for data set 2 do not differ substantially, and are shown in Supplementary Figs. S3–S5. Table 2 further lists the average electrical conductivity, and the root-mean-square (*rms*), minimum, and maximum in the relative conductivity anomalies estimated from the HS geometric average. Figs. 4–6 and Table 2 indicate that the electrical conductivity obtained for purely thermal and thermo-chemical models strongly differ, both in distribution pattern and

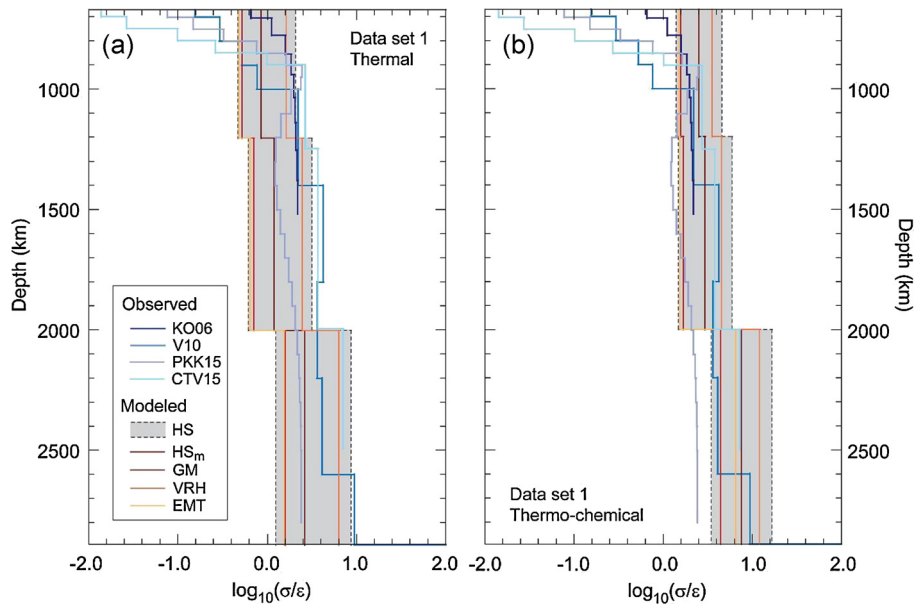


Fig. 4. Radial models of electrical conductivity for mineral physics data set 1 for (a) a purely thermal structure, and (b) a thermo-chemical structure. In each case, the grey shaded area extends from the lower to the upper Hashin–Shtrikman (HS) bound, and four estimators are shown: geometric average of upper and lower HS bounds (HS_m); geometric average (GM); Voigt–Reuss–Hill average (VRH); and effective medium theory (EMT). For comparison, four radial models based on magnetic field data, [Kuvshinov and Olsen \(2006\)](#) (KO06), [Velímský \(2010\)](#) (V10), [Puethe et al. \(2015\)](#) (PKK15), and [Civet et al., 2015](#) (CTV15) are also shown. Conductivity is plotted in logarithmic scale with $\epsilon = 1.0$ S/m.

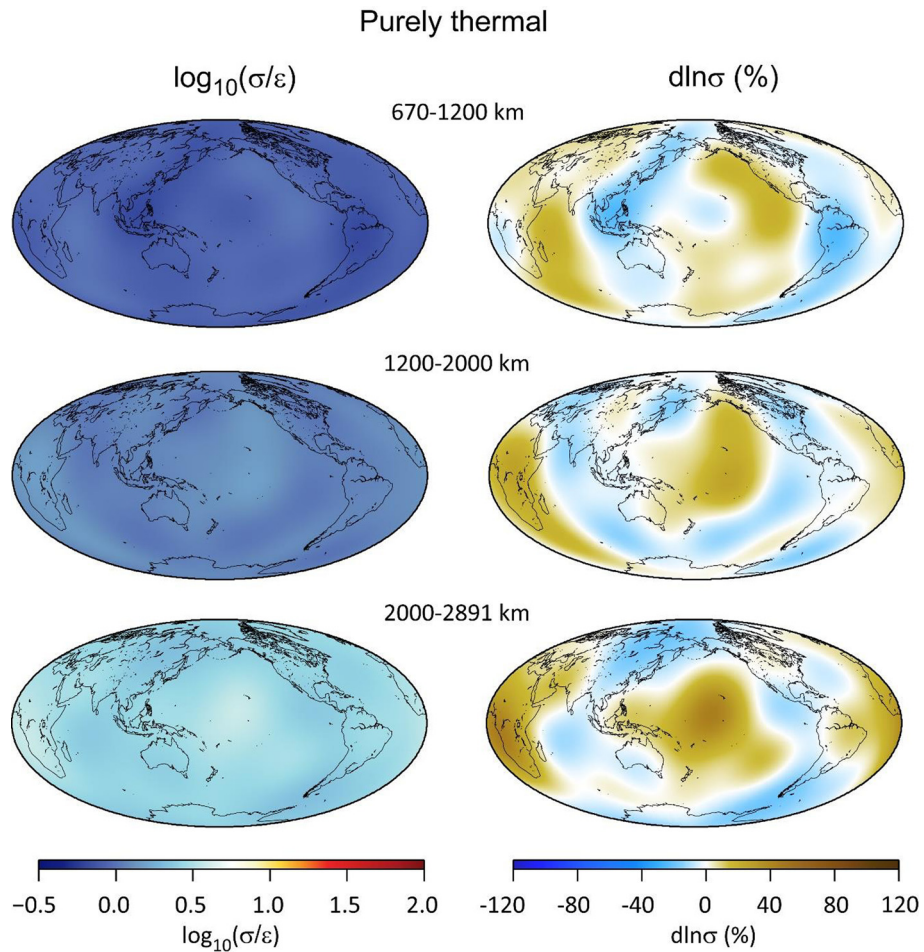


Fig. 5. Electrical conductivity inferred from a purely thermal model and mineral physics data set 1 in [Table 1](#), for layers 670–1200 km (top row), 1200–2000 km (middle row), and 2000–2891 km (bottom row). The thermal model is derived from the shear-wave velocity anomalies of probabilistic tomography ([Trampert et al., 2004](#)). Left and right columns show the logarithm (with $\epsilon = 1.0$ S/m) and relative anomalies in conductivity, respectively. Aggregate conductivity is calculated from the geometric average of Hashin–Shtrikman bounds. See Supplementary Figs. S6 to S8 for other estimators.

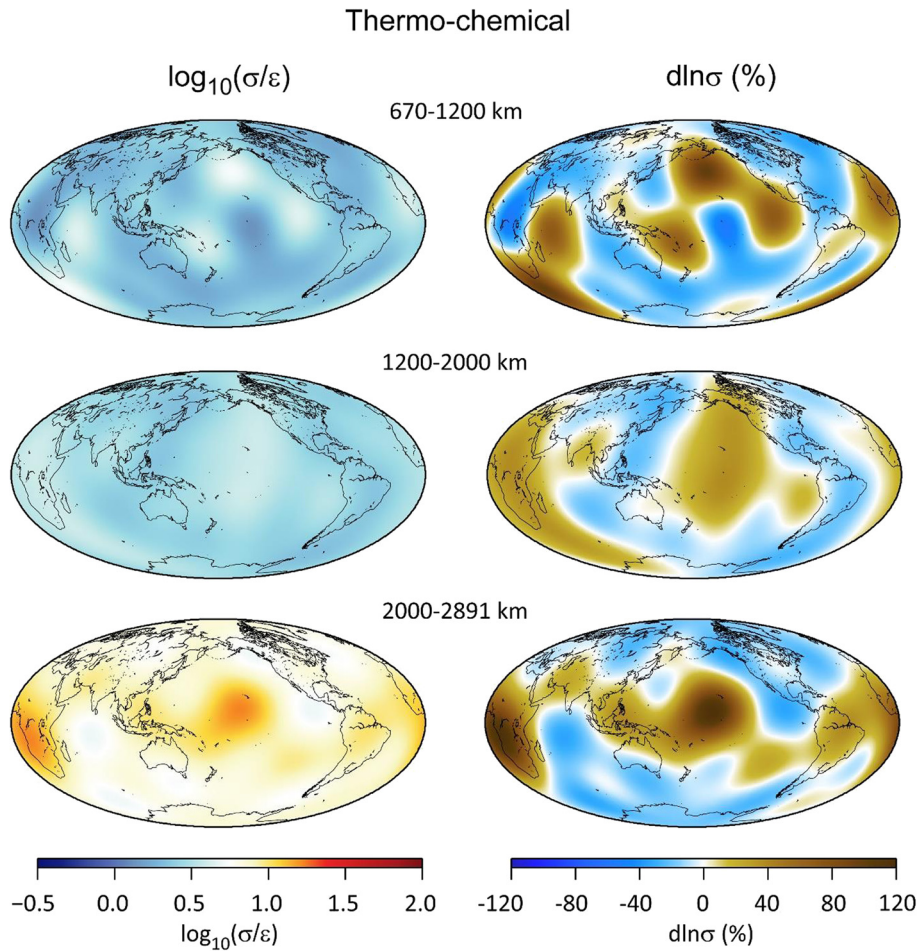


Fig. 6. Electrical conductivity inferred from the thermo-chemical 3D model of probabilistic tomography (Trampert et al., 2004) and mineral physics data set 1 in Table 1, for layers 670–1200 km (top row), 1200–2000 km (middle row), and 2000–2891 km (bottom row). Left and right columns show the logarithm (with $\varepsilon = 1.0$ S/m) and relative anomalies in conductivity, respectively. Aggregate conductivity is calculated from the geometric average of Hashin–Shtrikman bounds. See Supplementary Figs. S9 to S11 for other estimators.

Table 2
Statistics on the modeled lower mantle electrical conductivity for different models.

Mantle structure	Mineralogical data set	Layer (km)	σ_m (S/m)	$\delta\sigma$ (%)		
				<i>rms</i>	min	max
Purely thermal	1	670–1200	0.85	9.5	–24.4	82.6
		1200–2000	1.18	9.4	–14.8	78.6
		2000–2891	2.63	13.4	–19.7	67.0
Purely thermal	2	670–1200	1.05	9.3	–23.7	83.4
		1200–2000	1.24	9.6	–15.1	78.6
		2000–2891	2.27	14.7	–21.6	64.5
Thermo-chemical	1	670–1200	2.39	26.3	–44.4	104.5
		1200–2000	2.85	14.9	–24.8	36.0
		2000–2891	7.15	26.6	–30.8	119.8
Thermo-chemical	2	670–1200	2.51	28.8	–47.5	117.9
		1200–2000	2.51	15.8	–26.2	39.4
		2000–2891	5.13	26.6	–30.0	119.9

Listed values are the mean in electrical conductivity, and the root-mean-square (*rms*), minimum, and maximum in the relative anomalies in electrical conductivity. Electrical properties for mineralogical data sets 1 and 2 are listed in Table 1. Corresponding models are shown in Figs. 4 to 6 for data set 1, and Supplementary Figs. S2 to S4 for data set 2.

in amplitude. On average, purely thermal models predict electrical conductivity to be lower than that obtained for thermo-chemical models by a factor 2.5 to 3.0 (Table 2 and Fig. 4). It should be noted that comparisons between two given models are meaningful only if these models were calculated with the same estimator. The fact that the range covered by the HS bounds for purely thermal and thermo-chemical models overlap does not mean that these models are not substantially different. In the absence of knowl-

edge of the geometric distribution of minerals in the aggregate, HS bounds may be considered as uncertainties, keeping in mind that these uncertainties do not account for other sources of errors (e.g., uncertainties associated with mineral physics parameters). For the thermo-chemical model and data set 1, the mean conductivity estimated from the HS geometric average is close to 3.0 S/m in the mid-mantle (1200–2000 km) and around 7.0 S/m in the bottom part (2000–2891 km), in good agreement with several radial mod-

els obtained from inversion of magnetic field data (Kuvshinov and Olsen, 2006; Velínský, 2010; Civet et al., 2015). Interestingly, these observed profiles remain within the HS bounds throughout the lower mantle, except in its topmost part (Fig. 4b). By contrast, for the purely thermal model, the mean conductivity is around 1.0 S/m down to 2000 km and 2.6 S/m below, which agrees with the radial profiles of Pueche et al. (2015), but is somewhat smaller than the other observed profiles (Fig. 4a). The patterns and amplitude of relative lateral variations in electrical conductivity predicted by purely thermal and thermo-chemical models are also clearly different. Lateral variations in conductivity induced by purely thermal models are about half those induced by thermo-chemical models (Table 2 and Figs. 5 and 6). The difference in distribution patterns is more pronounced in the bottom layer, where the compositional variations from probabilistic tomography are the strongest. The discrepancies between purely thermal and thermo-chemical models result from the fact that variations in iron content, which are absent in purely thermal models, have a stronger influence on conductivity than the variations in temperature (Fig. 2). Different estimators lead to strong differences in the amplitude of the predicted conductivity, as illustrated by the strong differences in the horizontally-averaged conductivity models (Fig. 4). In contrast, the relative conductivity patterns remain mostly unchanged (Supplementary Figs. S6 to S11).

A striking feature that is present in thermo-chemical models for both mineral physics data sets and for all estimators, but not in purely thermal models, is a belt of high electrical conductivity running along the equator (bottom row in Fig. 6, Supplementary Fig. S11). The conductivity is peaking in the LLSVPs, with maximum values (for data set 1) of the HS geometric average around 16 S/m, leading to relative anomalies up to $\sim 120\%$ (Table 2). For the VRH and EMT averages, conductivity peaks at 20 S/m and 12 S/m, respectively, leading to maximum relative anomalies of 97% and 90%.

The strong differences in the electrical conductivity maps obtained for purely thermal and thermo-chemical models of lower mantle should result in strong differences between their respective electromagnetic response functions (C-responses). In the following, we investigate how far these responses can be used as a means to distinguish between these models.

4. C-responses

External variations of the magnetic field induce electrical currents in the conductive regions of the mantle. These currents in turn induce additional variations of the magnetic field that can be observed at the surface, with sounding depth increasing with period. Separating the external and internal variations of the magnetic field allows the calculation of the mantle response to a given input magnetic field variation, or C-response (e.g. Banks, 1969). At each frequency $\omega = 2\pi/T$, where T is period, and assuming that the source has a P_0^1 structure, the observed C-response is given by

$$C(\omega) = -\frac{a \tan \vartheta Z(\omega)}{2 H(\omega)}, \quad (11)$$

where $a = 6371.2$ km is Earth's mean radius, ϑ geomagnetic colatitude, and $Z(\omega)$ and $H(\omega)$ vertical and horizontal components of the magnetic field, respectively. C-responses depend on the distribution of electrical conductivity in the mantle, and can thus be used to constrain this distribution. Alternatively, theoretical C-responses may be calculated from *a priori* conductivity models.

We calculated C-responses from our 1D and 3D electrical conductivity models in the period range 3.0×10^5 – 10^8 s (4 to 730 days), which are sensitive to depths down to the core-mantle boundary. We further considered a hybrid model built from the top (670–1200 km) and middle (1200–2000 km) layers of the

purely thermal model, and the bottom layer (2000–2891 km) of the thermo-chemical model, accounting for the fact that, as a result of mantle early partial differentiation, lateral variations in composition may be significant in the lowermost mantle only. In all cases, we assumed that the crust and upper mantle (0–670 km) electrical conductivity is distributed in radially symmetric shells, with conductivity within each shell being given by the 1D model of Velínský (2010) (Fig. 4). To account for the fact that strong lateral variations in conductivity occur in the crust and uppermost mantle (>200 km), we tested other 1D models of upper mantle conductivity, but found that C-responses do not substantially depend on this parameter (Fig. S12). The largest differences appear at periods shorter than 10^6 s (12 days). At longer periods, the differences between C-responses obtained for different models of upper mantle conductivity are very small, and more importantly, they are always smaller than the differences between the C-responses for purely thermal and thermo-chemical models. The calculation of C-responses follows the method described in Kuvshinov (2008), which computes the magnetic field induced by a time-varying source (in our case, a magnetospheric ring current) exciting a given 3D-spherical distribution of electrical conductivity. Assuming that the source can be transferred to the frequency domain using a Fourier transform, the magnetic and electric fields, \mathbf{H} and \mathbf{E} , satisfy Maxwell's equations,

$$\nabla \times \mathbf{H} = \sigma \mathbf{E} + \mathbf{j}^{\text{ext}} \quad (12)$$

and

$$\nabla \times \mathbf{E} = i\omega\mu_0\mathbf{H}, \quad (13)$$

where σ is the conductivity model, \mathbf{j}^{ext} is the source current, $i = \sqrt{-1}$, ω is the frequency, and μ_0 is the magnetic permeability of space. In the region between the conducting Earth (i.e. for radius larger than the Earth's radius) and the external magnetospheric sources, the Fourier component $\mathbf{B}(\omega)$ of the magnetic field can be derived from a magnetic scalar potential V that may be expanded in spherical harmonics,

$$\mathbf{B}(\omega) = \mu_0\mathbf{H}(\omega) = -\nabla V(\omega), \quad (14)$$

$$V(r, \vartheta, \varphi, \omega)$$

$$= a \sum_{n=1}^{\infty} \sum_{m=-n}^n \left[\varepsilon_n^m(\omega) \left(\frac{a}{r}\right)^n + l_n^m(\omega) \left(\frac{a}{r}\right)^{n+1} \right] P_n^m(\cos \vartheta) e^{im\varphi}, \quad (15)$$

where r , ϑ , φ are radius, colatitude, and longitude in the geomagnetic coordinate system, $\varepsilon_n^m(\omega)$ and l_n^m the complex spherical harmonic coefficients of the inducing and induced parts of the magnetic potential, respectively, and $P_n^m(\cos \vartheta)$ Legendre polynomials. It is important to note that the radial component of the magnetic field is more affected by the induced current than the horizontal component, allowing C-responses (Eq. (11)) to be sensitive to the conductivity structure. The method used to solve Maxwell's equations allows the source to be located anywhere outside the conducting Earth. In our case, this source is the magnetospheric ring current, and we modeled it with a sheet current flowing at the surface of the Earth ($r = a$) with a P_0^1 structure in the geomagnetic coordinate system, corresponding to a large ring current symmetric to the geometric equator. For 1D conductivity models, Maxwell's equations may be solved using an iterative process (e.g. Srivastava, 1966). For 3D conductivity models, the calculation of electric and magnetic fields follows the 3D volume integral equation approach detailed in Kuvshinov (2008). This approach reduces Maxwell's equations to integral equations of the second kind (scattering equations) that are solved using appropriate (dyadic) Green's functions and conjugate gradients techniques.

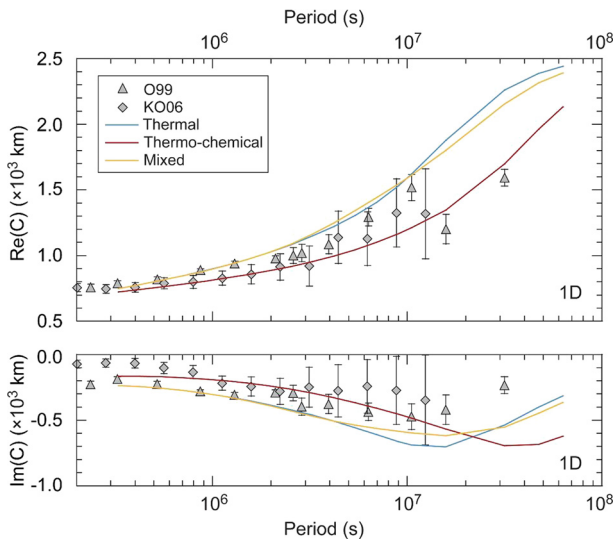


Fig. 7. Real (top) and imaginary (bottom) parts of C-responses calculated for 1D horizontally averaged purely thermal and thermo-chemical models of electrical conductivities (geometric average of Hashin–Shtrikman bounds) obtained with mineral physics data set 1. The mixed model is built from the top (670–1200 km) and middle (1200–2000 km) layers of the purely thermal model, and the bottom layer (2000–2891 km) of the thermo-chemical model. Symbols represent C-responses measured by Olsen (1999) (O99) from European geomagnetic observatories, and by Kuvshinov and Olsen (2006) (KO06) from of satellite data.

Fig. 7 shows the C-responses calculated for the horizontally averaged (1D) models obtained using the geometric mean of HS bounds (Fig. 4). For comparison, we also show the average C-responses computed from European geomagnetic observatory data (Olsen, 1999) and the global C-responses from 5 years of satellite data (Kuvshinov and Olsen, 2006). Fig. 8 plots the C-responses calculated at 5 locations corresponding to permanent geomagnetic observatories for the 3D conductivity models obtained using the geometric mean of HS bounds and mineral physics data set 1 (Figs. 5 and 6). Note that to better distinguish the real and imaginary parts, we plot imaginary parts with a minus sign. For comparison, C-responses obtained from geomagnetic data recorded at five selected observatories distributed across the globe (Australia, North America, Europe, China, and South Africa) (Khan et al., 2011), are also plotted. Two important conclusions may be drawn from our calculated C-responses. First, for the 1D model and for all the locations we considered, the real and imaginary parts of the C-responses predicted by the purely thermal and thermo-chemical models are clearly different for periods of 10^6 s (12 days) and higher. These differences appear for all estimators we considered (Fig. S13), as well as for the models calculated using data set 2 (Supplementary Figs. S14 and S15). C-responses for purely thermal and hybrid models are close to one another up to periods of 10^7 s (4 months), and differs significantly at longer periods. These differences, however, remain however small compared to those between the purely thermal and thermo-chemical models. Observed C-responses with period longer than a few months may thus provide a constraint on the thermo-chemical structure of the lower mantle, allowing to discriminate between a purely thermal structure, and the presence of both thermal and compositional anomalies. Second, for the 3D thermo-chemical models, the real parts of the C-responses vary significantly depending on the location, as indicated by their deviations from the C-response obtained for the 1D thermo-chemical model (Fig. 7 and dashed curves in Fig. 8). For the purely thermal and hybrid models, lateral variations in the 3D C-response are less pronounced and only visible at Tucson (TUC) and Honolulu (HON). Note that the largest deviations are found in Honolulu, which is located above conductivity highs through-

out the mantle for both the purely thermal and thermo-chemical models (Figs. 5 and 6). Again, deviations between the 3D and 1D C-responses suggest that comparison between local and globally-averaged observed C-responses may provide constraints on the pattern and amplitude of lateral anomalies in electrical conductivity in the lower mantle, and therefore on the nature and amplitude of the thermal and compositional variations that induce them.

A key question is whether the differences between the C-responses obtained for purely thermal and thermo-chemical models can be resolved by current magnetic field data. Horizontally-averaged C-responses have, so far, been measured for periods up to 3.0×10^7 s (1 year), corresponding to a sensitivity in depth up to ~ 1500 km. In the period range 10^7 – 3.0×10^7 s, and within their error bars, the horizontally averaged C-response obtained by Olsen (1999) (triangles in Fig. 7) fit the real part of the computed C-response built from the 1D thermo-chemical model reasonably well. These measurements, however, are still scarce, and may not be representative of the whole mantle. C-responses up to periods around 10^7 s have also been measured at several individual geomagnetic stations (Khan et al., 2011; Fig. 8). Within their current error bars, however, these C-responses cannot discriminate between the purely thermal and thermo-chemical models. This would require measurements with a better accuracy, leading to uncertainties in C-responses less than ~ 250 km at 10^7 s. Measurements at longer periods, up to about 2 years (6.0×10^7 s), would be needed to sample the lowermost mantle (≥ 2500 km), where differences between the purely thermal and thermo-chemical models are strongest. Reducing uncertainties in C-responses at periods longer than 10^7 s in turn requires series of geomagnetic data over longer time intervals (typically, several decades) to increase the coherence of the signal. Currently, the coherence is very low for periods longer than 10^7 s, leading to strong scattering in the C-responses (Khan et al., 2011).

5. Discussion

An important goal of this study was to build 3D maps of lower mantle electrical conductivity from possible 3D thermo-chemical models. Our maps are certainly affected by uncertainties in the mineral physics properties of lower mantle minerals. This includes uncertainties in the electrical properties and in the thermo-elastic properties, the latter being used to calculate the lower mantle thermo-chemical reference model and 3D structure from seismic models. The models plotted in Figs. 4 to 6 are thus means over large collections of models sampling the model space within their uncertainties. The standard deviations in these collections, which may be understood as first-order estimates of the uncertainties, are large, with *rms* (relative to horizontal average) around 60% and more, depending on layer and model.

Electrical conductivities of bridgmanite and ferropericlase may further depend on effects that are not accounted for in our dataset. In particular, the experiments of Yoshino et al. (2011) indicate that, due to iron spin crossover, the conductivity of ferropericlase slightly decreases in the pressure range 25–50 GPa, and increases again at larger pressure. Note, however, that these experiments were conducted at temperatures between 300 and 600 K. The detailed influence of iron spin crossover on lower mantle conductivity thus requires additional experiments at mantle temperatures. The presence of aluminum in bridgmanite may further influence the conductivity of this mineral. Sinmyo et al. (2014) found that the activation volume of Al-bridgmanite is lower than that of Al-free bridgmanite. At 82 GPa, their measurements indicate that the conductivity of bridgmanite with $X_{\text{Al}} = 0.06$ is larger than that of Al-free bridgmanite by about an order of magnitude. Recently, Yoshino et al. (2016) also reported an increase in the conductivity of bridgmanite with aluminum content. The presence of aluminum

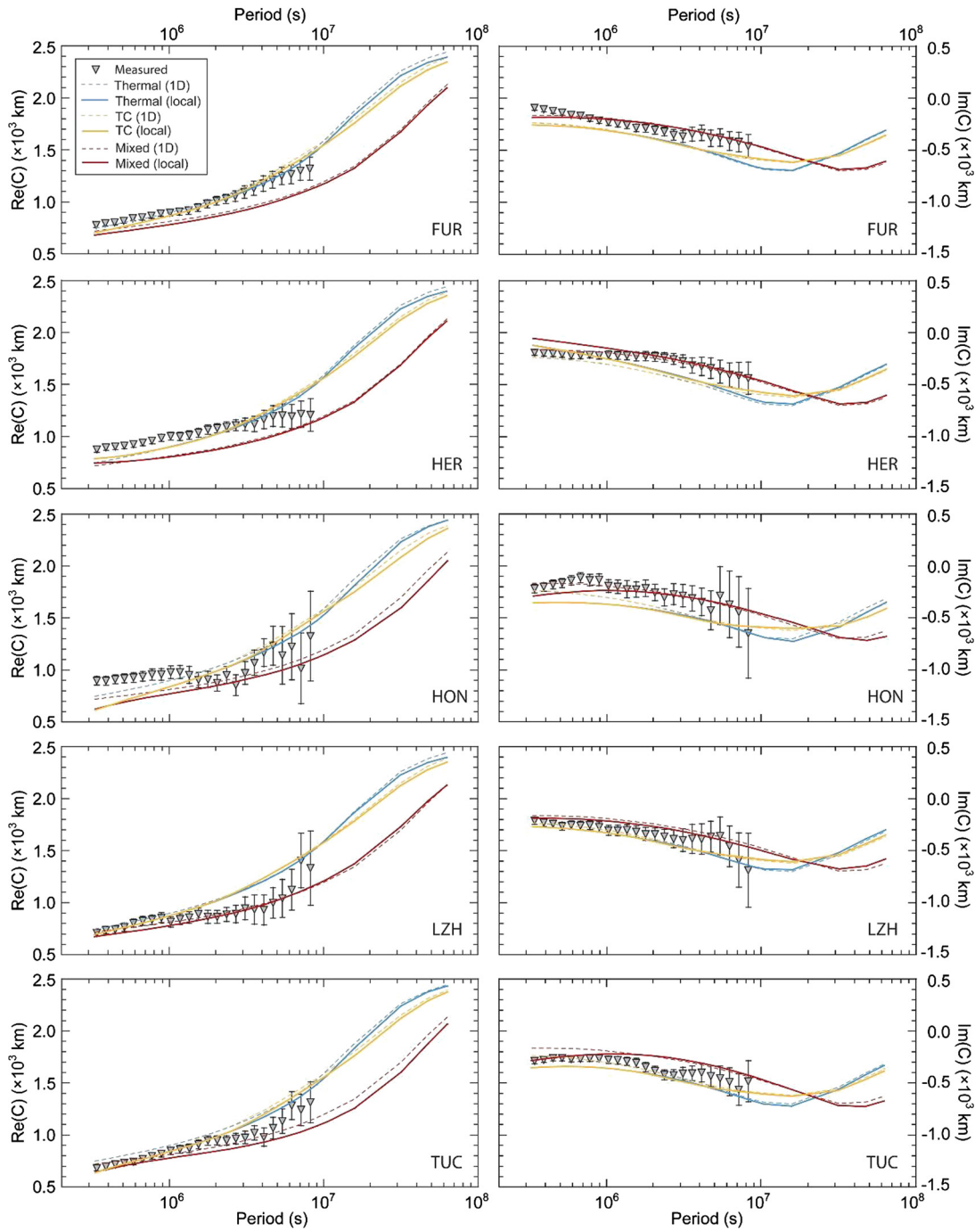


Fig. 8. Real (left column) and imaginary (right column) parts of C-responses calculated at 5 locations from 3D purely thermal and thermo-chemical models of electrical conductivities (geometric average of Hashin–Shtrikman bounds) obtained with mineral physics data set 1. Dashed curves show the corresponding C-response obtained for 1D models. The mixed model is built from the top (670–1200 km) and middle (1200–2000 km) layers of the purely thermal model, and the bottom layer (2000–2891 km) of the thermo-chemical model. Locations are Fürstenfeldbrück (FUR), Hermanus (HER), Honolulu (HON), Langzhou (LZH), and Tucson (TUC). Symbols represent measured C-responses at individual stations (Khan et al., 2011).

would then reduce the difference in conductivity between bridgmanite and ferropericlase, and therefore the sensitivity of lower mantle conductivity to changes in the fraction of bridgmanite.

The lower mantle thermo-chemical model of Trampert et al. (2004), which we used here, assumes that compositional anomalies in the lowermost mantle are dominated by lateral variations in the amount of iron and silicate. This assumption explains well the anti-correlation between shear-wave and bulk-sound velocity anomalies, and is consistent with the hypothesis that LLSVPs result from an early chemical differentiation of the mantle (Nomura

et al., 2011). Our maps of electrical conductivity do not account for other potential sources of chemical heterogeneities, in particular high-pressure MORB that may be entrained in the deep mantle by subducted slabs. Unless very hot compared to the surrounding mantle, high-pressure MORB alone is unlikely to explain LLSVPs (Deschamps et al., 2012). It may, however, be present in local pools around LLSVPs or even be incorporated in small amounts within LLSVPs, as suggested by the BAM model (Tackley, 2012). Compared to pyrolite, MORB is enriched in iron and should therefore be more conductive than the pyrolitic mantle. According to the experiments

of Ohta et al. (2010), the electrical conductivity of MORB strongly increases with pressure. It varies between 3 and 10 S/m at 51 GPa (1200 km depth) and for temperatures in the range 1400–2100 K, and increases to 300 S/m at 133 GPa and 2500 K, *i.e.* more than one order of magnitude larger than the maximum electrical conductivity of our thermo-chemical model (Fig. 6). High pressure MORB may, however, only be present in limited amounts in the lowermost mantle, and part of it may be incorporated in LLSVPs (Tackley, 2012), thus decreasing its global effect. It should further be pointed out that large increases triggered by the presence of recycled MORB would affect the 1D radial profile of electrical conductivity, inducing a sharp increase at the bottom of the mantle. Such an increase is not seen in the radial 1D model of Velímský (2010).

The presence of post-perovskite may further affect the distribution of electrical conductivity at the bottom of the mantle. Mineral physics experiments (Ohta et al., 2008) suggest that the electrical conductivity of post-perovskite at 129 GPa and 2500 K is around 50 S/m, *i.e.* larger than the peak value of our models by about a factor three. However, it has been found that bridgmanite and post-perovskite may coexist in the lowermost mantle, but that post-perovskite would be depleted in iron compared to bridgmanite (Andraut et al., 2009). Sinmyo et al. (2011) reached a similar conclusion and showed that during the phase change from bridgmanite to post-perovskite, iron changes its valence from Fe³⁺ to Fe²⁺ and preferentially partitions to ferropericlasite. These effects would strongly decrease the conductivity of post-perovskite in the deep mantle. Furthermore, small lenses of post-perovskite may be present within LLSVPs (Li et al., 2016), in which case they would be enriched in iron due to the pressure and temperature conditions in these regions (Mao et al., 2006). Overall, the effective influence of post-perovskite on lowermost mantle electrical conductivity is complicated, and additional measurements are required for further analysis.

6. Conclusion

Despite the limitations discussed in section 5, our calculations indicate that mantle electrical conductivity is potentially a powerful tool to infer thermal and chemical variations in the lower mantle. In particular, we have shown that electrical conductivity is able to discriminate between purely thermal and thermo-chemical models. The patterns and amplitudes of electrical conductivity anomalies associated with purely thermal and thermo-chemical (in our case, iron and silicate anomalies) models are clearly different, with thermo-chemical models being on average more conductive than purely thermal models and leading to stronger lateral variations of electrical conductivity. A striking feature of the thermo-chemical models investigated here is the presence of a high conductivity belt in the lowermost mantle around the equator. These differences result in strong changes in the predicted C-responses, which should be resolvable by long-period variations of the magnetic field. In the case of thermo-chemical models, lateral variations in conductivity result in significant geographical variations in the computed C-responses, which, again, could be resolvable if high precision measurements of magnetic field variations at long-periods were available.

Acknowledgements

We are grateful to two anonymous colleagues for their constructive comments. This research was funded by Academia Sinica grant AS-102-CDA-M02 (FD). We would also like to thank Alexey Kuvshinov for informed discussions.

Appendix A. Supplementary material

Supplementary material related to this article can be found online at <http://dx.doi.org/10.1016/j.epsl.2016.06.027>.

References

- Andraut, D., Muñoz, M., Bolfan-Casanova, N., Guignot, N., Perrillat, J.-P., Anquilanti, G., Pascarelli, S., 2009. Experimental evidence for perovskite and post-perovskite coexistence throughout the whole D'' region. *Earth Planet. Sci. Lett.* 293, 90–96.
- Banks, R.J., 1969. Geomagnetic variations and electrical conductivity of the upper mantle. *Geophys. J. R. Astron. Soc.* 17, 457–487.
- Civet, F., Thébault, E., Verhoeven, O., Langlais, B., Saturnino, D., 2015. Electrical conductivity of the Earth's mantle from the first Swarm magnetic field measurements. *Geophys. Res. Lett.* 42, 3338–3346.
- Davies, D.R., Goes, S., Davies, J.H., Schuberth, B.S.A., Bunge, H.-P., Ritsema, J., 2012. Reconciling dynamic and seismic models of Earth's lower mantle: the dominant role of thermal heterogeneity. *Earth Planet. Sci. Lett.* 353–354, 253–269.
- Deschamps, F., 2015. Lower mantle electrical conductivity inferred from probabilistic tomography. *Terr. Atmos. Ocean. Sci.* 26, 27–40. [http://dx.doi.org/10.3319/TAO.2014.08.19.03\(GRT\)](http://dx.doi.org/10.3319/TAO.2014.08.19.03(GRT)).
- Deschamps, F., Trampert, J., 2004. Towards a lower mantle reference temperature and composition. *Earth Planet. Sci. Lett.* 222, 161–175.
- Deschamps, F., Cobden, L., Tackley, P.J., 2012. The primitive nature of large low shear-wave velocity provinces. *Earth Planet. Sci. Lett.* 349–350, 198–208.
- Dobson, D.P., Brodholt, J.P., 2000. The electrical conductivity of the lower mantle phase magnesiowüstite at high temperatures and pressures. *J. Geophys. Res.* 105, 531–538.
- Goddard, A., Peyronneau, J., Poirier, J.-P., 1999. Dependence on pressure of conduction by hopping of small polarons in minerals of the Earth's lower mantle. *Phys. Chem. Miner.* 27, 81–87.
- Hashin, Z., Shtrikman, S., 1962. A variational approach to the theory of the effective magnetic permeability of multiphase materials. *J. Appl. Phys.* 33, 3125–3131.
- Hill, R., 1963. Elastic properties of reinforced solids: some theoretical principles. *J. Mech. Phys. Solids* 11, 357–372.
- Ishii, M., Tromp, J., 1999. Normal-mode and free-air gravity constraints on lateral variations in velocity and density of Earth's mantle. *Science* 285, 1231–1236.
- Kelbert, A., Schultz, A., Egbert, G., 2009. Global electromagnetic induction constraints on transition-zone water content variations. *Nature* 460, 1003–1007.
- Khan, A., Connolly, J.A.D., Olsen, N., 2006. Constraining the composition and thermal state of the mantle beneath Europe from inversion of long-period electromagnetic sounding data. *J. Geophys. Res.* 111, B10102. <http://dx.doi.org/10.1029/2006JB004270>.
- Khan, A., Kuvshinov, A., Semenov, A., 2011. On the heterogeneous electrical conductivity structure of the Earth's mantle with implications for the transition zone water content. *J. Geophys. Res.* 116, B01103. <http://dx.doi.org/10.1029/2010JB007458>.
- Khan, A., Shankland, T.J., 2012. A geophysical perspective on mantle water content and melting: inverting electromagnetic sounding data using laboratory-based electrical conductivity profiles. *Earth Planet. Sci. Lett.* 317–318, 27–43.
- Khan, A., Koch, S., Shankland, T.J., Zunino, A., Connolly, J.A.D., 2015. Relationships between seismic wave-speed, density, and electrical conductivity beneath Australia from seismology, mineralogy, and laboratory-based conductivity profiles. In: Khan, A., Deschamps, F. (Eds.), *The Earth's Heterogeneous Mantle*. Springer Geophysics, pp. 145–171.
- Koyama, T., Khan, A., Kuvshinov, A., 2014. Three-dimensional electrical conductivity structure beneath Australia from inversion of geomagnetic observatory data: evidence for lateral variations in transition-zone temperature, water content, and melt. *Geophys. J. Int.* 196, 1330–1350. <http://dx.doi.org/10.1093/gji/ggt455>.
- Kuvshinov, A., 2008. 3D global induction in the oceans and solid Earth: recent progresses in modeling magnetic and electric fields from sources of magnetospheric, ionospheric and oceanic origins. *Surv. Geophys.* 29, 139–186. <http://dx.doi.org/10.1007/s10712-008-9045-z>.
- Kuvshinov, A., Olsen, N., 2006. A global model of mantle conductivity derived from 5 years of CHAMP, Ørsted, and SAC-C magnetic data. *Geophys. Res. Lett.* 33, L18301. <http://dx.doi.org/10.1029/2006GL027083>.
- Kuvshinov, A., Semenov, A., 2012. Global 3-d imaging of mantle conductivity based on inversion of observatory C-responses—I. An approach and its verification. *Geophys. J. Int.* 189, 1335–1352.
- Landauer, R., 1952. The electrical resistance of binary metallic mixtures. *J. Appl. Phys.* 23, 779–784.
- Li, Y., Deschamps, F., Tackley, P.J., 2016. Effects of the post-perovskite phase transition properties on the stability and structure of primordial reservoirs in the lower mantle of the Earth. *Geophys. Res. Lett.* 43, 3215–3225.
- Mao, W.-L., Mao, H.-K., Sturhahn, W., Zhao, J., Prakapenka, V.B., Meng, Y., Shu, J., Fei, Y., Hemley, R.J., 2006. Iron-rich post-perovskite and the origin of ultra-low velocity zones. *Science* 312, 564–565.
- Masters, G., Laske, G., Bolton, H., Dziewonski, A.M., 2000. The relative behavior of shear velocity, bulk sound speed, and compressional velocity in the mantle: implication for thermal and chemical structure. In: Karato, S.-I., et al. (Eds.), *Earth's*

- Deep Interior: Mineral Physics and Tomography from the Atomic to the Global Scale. In: Geophysical Monograph Ser., vol. 117. American Geophysical Union, Washington, DC, pp. 63–87.
- Mosca, I., Cobden, L., Deuss, A., Ritsema, J., Trampert, J., 2012. Seismic and mineralogical structures of the lower mantle from probabilistic tomography. *J. Geophys. Res.* 117, B06304. <http://dx.doi.org/10.1029/2011JB008851>.
- Nomura, R., Ozawa, H., Tateno, S., Hirose, K., Hernlund, J., Muto, S., Ishii, H., Hiraoka, N., 2011. Spin crossover and iron-rich silicate melt in the Earth's deep mantle. *Nature* 473, 199–203.
- Ohta, K., Onoda, S., Hirose, K., Sinmyo, R., Shimizu, K., Sata, N., Ohishi, Y., Yasuhara, A., 2008. The electrical conductivity of post-perovskite in Earth's D'' layer. *Science* 320, 89–91.
- Ohta, K., Onoda, S., Hirose, K., Sinmyo, R., Shimizu, K., Sata, N., Ohishi, Y., Yasuhara, A., 2010. Electrical conductivities of pyrolytic mantle and MORB materials up to the lowermost mantle conditions. *Earth Planet. Sci. Lett.* 289, 497–502.
- Olsen, N., 1999. Long-periods (30 days–1 year) electromagnetic sounding and the electric conductivity of the lower mantle beneath Europe. *Geophys. J. Int.* 138, 179–187.
- Poirier, J.-P., 1991. Introduction to the Physics of the Earth's Interior. Cambridge University Press, Cambridge. 264 pp.
- Poirier, J.-P., Peyronneau, J., 1992. Experimental determination of the electrical conductivity of the Earth's lower mantle. In: Syono, Y., Manghni, M.H. (Eds.), High-Pressure Research: Application to Earth and Planetary Sciences. In: Geophysical Monograph Ser., vol. 67. American Geophysical Union, Washington, DC, pp. 77–87.
- Puethé, C., Kuvshinov, A., Khan, A., Olsen, N., 2015. A new model of Earth's radial conductivity derived from over 10 yr of satellite and observatory magnetic data. *Geophys. J. Int.* 203, 1864–1872.
- Ritsema, J., Deuss, A., van Heijst, H.-J., Woodhouse, J.H., 2011. S40RTS: a degree–40 shear-velocity model for the mantle from new Rayleigh wave dispersion, teleseismic traveltimes and normal-mode splitting function measurements. *Geophys. J. Int.* 184, 1223–1236.
- Semenov, A., Kuvshinov, A., 2012. Global 3-D imaging of mantle conductivity based on inversion of observatory C-responses—II. Data analysis and results. *Geophys. J. Int.* 191, 965–992.
- Shankland, T.J., Duba, A.G., 1990. Standard electrical conductivity of isotropic, homogeneous olivine in the temperature range 1200°–1500°C. *Geophys. J. Int.* 103, 25–31.
- Shankland, T.J., Peyronneau, J., Poirier, J.-P., 1993. Electrical conductivity of the Earth's lower mantle. *Nature* 366, 453–455.
- Sinmyo, R., Hirose, K., Muto, S., Ohishi, Y., Yasuhara, A., 2011. The valence state and partitioning of iron in the Earth's lowermost mantle. *J. Geophys. Res.* 116. <http://dx.doi.org/10.1029/2010JB008179>.
- Sinmyo, R., Pesce, G., Greenberg, E., McCammon, C., Dubrovinsky, L., 2014. Lower mantle electrical conductivity based on measurements of Al, Fe-bearing perovskite under lower mantle conditions. *Earth Planet. Sci. Lett.* 393, 165–172.
- Srivastava, S.P., 1966. Theory of the magnetotelluric method for a spherical conductor. *Geophys. J. R. Astron. Soc.* 11, 373–387.
- Tackley, P.J., 2012. Dynamics and evolution of the deep mantle resulting from thermal, chemical, phase and melting effects. *Earth-Sci. Rev.* 110, 1–25.
- Trampert, J., Deschamps, F., Resovsky, J.S., Yuen, D.A., 2004. Probabilistic tomography maps significant chemical heterogeneities in the lower mantle. *Science* 306, 853–856.
- Vacher, P., Verhoeven, O., 2007. Modelling the electrical conductivity of iron-rich minerals for planetary applications. *Planet. Space Sci.* 55, 455–465.
- van der Hilst, R.D., Kárason, H., 1999. Compositional heterogeneity in the bottom 1000 kilometers of Earth's mantle: towards a hybrid convection model. *Science* 283, 1885–1888.
- Velínský, J., 2010. Electrical conductivity in the lower mantle: constraints from CHAMP satellite data by time-domain EM induction modeling. *Phys. Earth Planet. Inter.* 180, 111–117.
- Verhoeven, O., Mocquet, A., Vacher, P., Rivoldini, A., Menvielle, M., Arrial, P.-A., Choblet, G., Tarits, P., Dehant, V., van Hoolst, T., 2009. Constraints on thermal state and composition of the Earth's lower mantle from electromagnetic impedances and seismic data. *J. Geophys. Res.* 114, B03302. <http://dx.doi.org/10.1029/2008JB005678>.
- Xu, Y., McCammon, C., 2002. Evidence for ionic conductivity in lower mantle (Mg, Fe) (Si, Al)O₃ perovskite. *J. Geophys. Res.* 107. <http://dx.doi.org/10.1029/2002JB001783>.
- Xu, Y., McCammon, C., Poe, B.T., 1998. The effect of alumina on the electrical conductivity of silicate perovskite. *Science* 282, 922–924.
- Xu, Y., Shankland, T.J., Poe, B.T., 2000. Laboratory based electrical conductivity in the Earth's mantle. *J. Geophys. Res.* 105, 27865–27875.
- Yoshino, T., Matsuzaki, T., Shatskiy Katsura, T., 2009. The effect of water on the electrical conductivity of olivine aggregates and its implications for the electrical structure of the upper mantle. *Earth Planet. Sci. Lett.* 288, 291–300.
- Yoshino, T., Ito, E., Katsura, T., Yamazaki, D., Shan, S., Guo, X., Nishi, M., Higo, Y., Funakoshi, K.-I., 2011. Effect of iron content on electrical conductivity of ferropericlase with implications for the spin transition pressure. *J. Geophys. Res.* 116. <http://dx.doi.org/10.1029/2010JB007801>.
- Yoshino, T., Kamada, S., Ito, E., Hirao, N., 2016. Electrical conductivity model of Al-bearing bridgmanite with implications for the electrical structure of the Earth's lower mantle. *Earth Planet. Sci. Lett.* 434, 208–219.